

Following reaction of isolate 22 with BMCC, the RNA was isolated by gel filtration and digested with ribonuclease I. The sample was then purified by high-performance liquid chromatography (HPLC) and subjected to electrospray-ionization tandem quadrupole mass spectrometry. From the resulting data, the ion corresponding to the Diels–Alder product was identified (measured M_r , 630.6; calculated M_r , 630.8). Moreover, many additional fragment ions were observed which further substantiate formation of the Diels–Alder product. No ions were observed for BMCC reacting with any functional groups on the oligonucleotide, consistent with only the formation of the Diels–Alder cycloadduct.

The methodology used to create these RNA DAases provides a straightforward approach to generating novel catalysts on demand that do not require templating of either substrate. The scope of RNA-catalysed reactions now includes carbon–carbon bond-forming reactions. Although no examples of RNA-catalysed carbon–carbon bond formation were previously known, there appear to be many solutions to $[4 + 2]$ cycloaddition catalysis, as eight unique sequences were found that enhance the rate of the Diels–Alder reaction. These results suggest that similar strategies could be used to identify RNA molecules that catalyse other Diels–Alder reactions, including those with typically unreactive substrates, inverse electron demand Diels–Alder cycloadditions, and hetero Diels–Alder reactions. RNA catalysis of other types of cycloaddition reactions such as dipolar cycloadditions, particularly those benefiting from Lewis acid catalysis, are also possibilities. The ability to expand greatly the functional diversity of RNA through modified bases, to augment accessible chemistries through the use of transition metals, and, perhaps in the future, to include co-factor-assisted transformations, has significant implications for the range of reactions amenable to RNA catalysis. □

Methods

Incubation conditions. The RNA–PEG–diene construct was prepared by ligating on a PEG–diene modified DNA 10-mer to the 5' end of the RNA using T4 DNA ligase. All RNA incubations were conducted under the following conditions except as noted: 50 mM HEPES, pH 7.0, 500 nM pyridyl methyl-modified RNA, 200 mM NaCl, 200 mM KCl, 1 mM CaCl_2 , 1 mM MgCl_2 , 10 μM each aluminium lactate, $\text{Ga}_2(\text{SO}_4)_3$, MnCl_2 , FeCl_2 , CoCl_2 , NiCl_2 , CuCl_2 and ZnCl_2 , 10% ethanol and 2% dimethyl sulphoxide. The concentration of dienophile 1 (BMCC) varied in the isolate characterization experiments, but was held constant at 100 μM throughout the SELEX. Incubations were terminated by the addition of β -mercaptoethanol to a final concentration of 5 mM and/or passing the solution over two successive Nap columns (Pharmacia) to remove excess BMCC.

Reaction assay and partitioning. The extent of reaction and partitioning of reacted and unreacted RNA molecules was accomplished using a streptavidin (SA) dependent gel shift. The shifted and unshifted bands were visualized by autoradiography and phosphor-imaging, the latter being used for quantification. For partitioning, shifted bands were excised, the RNA–SA complex extracted, desalted and subjected to reverse transcription and PCR amplification according to standard procedures.

Kinetic analyses. All data were obtained at 500 nM RNA and the indicated amounts of BMCC. k_{obs} values were determined by fitting the fraction of unreacted RNA to the equation for first-order kinetics. The uncatalysed second-order rate of Diels–Alder reaction was measured using random pyridine-modified RNA ($k_{\text{uncat}} = 5.42 \times 10^{-3} \text{ M}^{-1} \text{ s}^{-1}$).

Product inhibition. Apparent K_i values for the free cycloaddition product 3 were determined at 500 μM BMCC by fitting the observed first-order rate constants to the following equation for inhibition: $k_{\text{obs}} = (k_{\text{obs0}}/2)(\alpha E - I - K_i + ((K_i + \alpha E - I)^2 + 4K_i)^{1/2})$ where k_{obs} is the measured rate constant in the presence of 3, k_{obs0} is the observed rate constant in the absence of 3, αE represents the fractional (α) concentration of functional active sites (E), I is the concentration of 3, and K_i is the apparent inhibition constant.

Received 23 April; accepted 22 July 1997.

- Joyce, G. F. Ribozymes: Building the RNA world. *Curr. Biol.* **6**, 965–967 (1996).
- Joyce, G. F. The rise and fall of the RNA world. *New Biologist* **3**, 399–407 (1991).

- Joyce, G. F. Some biochemical thoughts on the RNA world. *Chem. Biol.* **3**, 405–407 (1996).
- Cech, T. R. The chemistry of self-splicing RNA and RNA enzymes. *Science* **236**, 1532–1539 (1987).
- Long, D. M. & Uhlenbeck, O. C. Self-cleaving catalytic RNA. *FASEB J.* **7**, 25–30 (1993).
- Bartel, D. P. & Szostak, J. W. Isolation of new ribozymes from a large pool of random sequences. *Science* **261**, 1411–1418 (1993).
- Beaudry, A. A. & Joyce, G. F. Directed evolution of an RNA enzyme. *Science* **257**, 635–641 (1992).
- Kumar, P. K. R. & Ellington, A. D. Artificial evolution and natural ribozymes. *FASEB J.* **9**, 1183–1195 (1995).
- Illangasekare, M., Sanchez, G., Nickles, T. & Yarus, M. Aminoacyl-RNA synthesis catalyzed by an RNA. *Science* **267**, 643–647 (1995).
- Lohse, P. A. & Szostak, J. W. Ribozyme-catalyzed amino-acid transfer reactions. *Nature* **381**, 442–444 (1996).
- Li, Y. & Sen, D. A catalytic DNA for porphyrin metallation. *Nature Struct. Biol.* **3**, 743–747 (1996).
- Conn, M. M., Prudent, J. R. & Schultz, P. G. Porphyrin metallation catalyzed by a small RNA molecule. *J. Am. Chem. Soc.* **118**, 7012–7013 (1996).
- Dewey, T. M., Zyzanski, C. & Eaton, B. E. The RNA world: functional diversity in a nucleoside by carboxyamidation of uridine. *Nucleosides & Nucleotides* **15**, 1611–1617 (1996).
- Morris, K. N. *et al.* Enrichment for RNA molecules that bind a Diels–Alder transition state analog. *Proc. Natl Acad. Sci. USA* **91**, 13028–13032 (1994).
- Jencks, W. P. in *Catalysis in Chemistry and Enzymology* 644–712 (Dover Publications, New York, 1987).
- Williams, J. W. & Morrison, J. F. The kinetics of reversible tight-binding inhibition. *Methods Enzymol.* **63**, 437–467 (1979).
- Kazakov, S. A. in *Bioorganic Chemistry: Nucleic Acids* (ed. Hecht, S. M.) 244 (Oxford Univ. Press, New York, 1996).
- Cotton, F. A. & Wilkinson, G. *Advanced Inorganic Chemistry* (Wiley, New York, 1988).
- Otto, S., Bertocini, F. & Engberts, J. B. F. N. Lewis acid catalysis of a Diels–Alder reaction in water. *J. Am. Chem. Soc.* **118**, 7702–7707 (1996).
- Otto, S. & Engberts, J. B. F. N. Lewis acid catalysis of a Diels–Alder reaction in water. *Tetrahed. Lett.* **36**, 2645–2648 (1995).
- Ni, J., Pomerantz, S. C., Rozenski, J., Zhang, Y. & McCloskey, J. M. Interpretation of oligonucleotide mass spectra for determination of sequence using electrospray ionization and tandem mass spectrometry. *Anal. Chem.* **68**, 1889–1899 (1996).
- Pomerantz, S. C., McCloskey, J. A., Tarasow, T. M. & Eaton, B. E. Deconvolution of combinatorial oligonucleotide libraries by electrospray ionization tandem mass spectrometry. *J. Am. Chem. Soc.* **119**, 3861–3867 (1997).
- Tarasow, T., Tinnermeier, D. & Zyzanski, C. Characterization of oligodeoxyribonucleotide-polyethylene glycol conjugates by electrospray mass spectrometry. *Bioconjugate Chem.* **8**, 89–93 (1997).
- Wiegand, T. W., Janssen, R. C. & Eaton, B. E. Selection of RNA amide synthases. *Chem. Biol.* (in the press).

Acknowledgements. We thank L. Gold for support, guidance and vision; the scientific community at NeXstar, especially members of the Medicinal Chemistry group, for helpful discussions and ideas; S. Wayland for the synthesis of compound 2; and T. Wiegand and D. Nieuwlandt for inspiring dialogue and technical assistance. We also thank S. C. Pomerantz, P. F. Crain and J. A. McCloskey for ESI–MS/MS analysis.

Correspondence and requests for materials should be addressed to B.E.E. (e-mail: beaton@nexstar.com).

Abrupt mid-twentieth-century decline in Antarctic sea-ice extent from whaling records

William K. de la Mare

Australian Antarctic Division, Department of the Environment, Sport and Territories, Channel Highway, Kingston, Tasmania 7050, Australia

A decline in Antarctic sea-ice extent is a commonly predicted effect of a warming climate. Direct global estimates of the Antarctic sea-ice cover from satellite observations, only possible since the 1970s^{1–4}, have shown no clear trends. Comparisons¹ between satellite observations and ice-edge charts obtained from early ship records⁵ suggest that sea-ice extent in the 1970s was less than during the 1930s, an indication supported by limited regional observations⁶. But these observations have been regarded as inconclusive, owing to the limited spatial and temporal scope of the early records². A significant data source has, however, been overlooked. The southern limit of whaling was constrained by sea ice, and since 1931 whaling records have been collected for every whale caught⁷, giving a circumpolar coverage from spring to autumn until 1987. Here, an analysis of these catch records indicates that, averaged over October to April, the Antarctic summer sea-ice edge has moved southwards by 2.8° of latitude between the mid 1950s and early 1970s. This suggests a decline in the area covered by sea ice of some 25%. This abrupt change poses a challenge to model simulations of recent climate change, and could imply changes in Antarctic deep-water formation and in biological productivity, both important processes affecting atmospheric CO₂ concentrations.

Whaling in the Antarctic began in 1904 from land stations and in 1905 the first floating factories were introduced. The early factory ships lacked slipways for hauling whales on board, but they could process the catch by mooring to an ice floe, leading to the fortuitous discovery that whales, especially the highly prized blue whales, tended to concentrate near the ice edge⁷. The sea-ice margin is an area of enhanced biological productivity^{8,9}, and pelagic whaling concentrated near the ice edge for most of the commercial era. The introduction of floating factories with stern slipways led to the expansion of whaling around Antarctica, and by 1931 the pattern of whaling near the ice edge was well established¹⁰. The whaling season usually began in October and continued through the Antarctic summer until April. The whaling fleets spread along the ice edge at the start of the season, following it southwards as it retreated¹⁰. No pelagic whaling occurred from 1940 to 1946, but after the Second World War catching again concentrated near the ice edge. From 1957 to 1975, the scarcity of blue, fin and humpback whales led to whaling concentrating on sei whales in the region of the South Polar Front, well north of the ice edge¹¹. In 1972 whaling turned to the remaining abundant species, the relatively small minke whale. As with blue, fin and humpback whaling, minke whaling occurred near the ice edge¹², and became widespread until the end of commercial whaling after 1986/87.

The International Whaling Commission has entered about 1.5 million catch records into computer files from logbooks submitted to the Bureau of International Whaling Statistics in Norway. The data recorded for each whale include the species, date of capture and the noon position of the factory ship (to at least the nearest degree of latitude and longitude). I used a database program to extract the records for the southernmost catch for each unique longitude and date. The data from land stations at South Georgia were excluded, as were catches after the 1956/57 season for species other than minke whales. This resulted in 42,258 records. No records satisfied the selection criteria from 1960 to 1971 inclusive, when sei whaling

predominated. The mean latitudes of the southernmost catches were calculated for each combination of three independent factors; the 10° longitudinal sector ('sector'), 10-day period ('decade') and season ('year'). Three decades within each month were defined by the days 1–10, 11–20, >20. The data were censored to exclude any positions more than 3° north of the southernmost position for each factor combination. There were 38 seasons, 19 decades and 36 sectors, leading to 25,992 combinations. Not all combinations are represented in the data; 4,424 combinations have an observed mean southernmost catch latitude. The seasons were in three sections, 1931/32 to 1940/41, 1946/47 to 1958/59 and 1971/72 to 1986/87. The dates within seasons ranged from 14 October to April 20.

An analysis of variance was carried out using a generalized linear model with an identity link function and normal errors¹³, with the mean southernmost catch latitude as the dependent variable. Only main effects were estimated because there is only one observation per cell. The observations cross the levels of the three factors sufficiently for all the coefficients of the linear model to be estimatable. The analysis of variance table (Table 1) shows that each factor is statistically significant.

The mean effect due to a given factor can be plotted as the predicted value of the dependent variable, and its standard error, for each level of the given factor, with the other factors held fixed. Figure 1 shows the predicted mean latitude of the southernmost catches by year. The mean latitudes for the southernmost catches were roughly constant in the period 1931–54 with a mean of 61.5° S. In the mid 1950s the catch latitudes begin to move southward, although the pattern of the change cannot be estimated during the period of sei whaling. From 1973 onwards the latitude is again roughly stable, but 2.8° further south, with a mean of 64.3° S.

A plot of the average catch latitude by time of year showed a smooth curve corresponding to the seasonal pattern of the retreat and advance of the sea ice, with a minimum estimated to occur in the first decade in March (see Supplementary Information). Figure 2

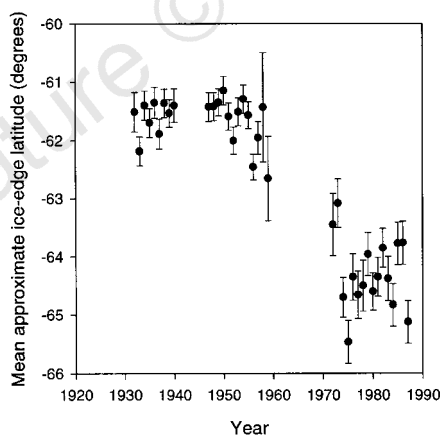


Figure 1 Mean approximate ice-edge latitude in Antarctica from 1931 to 1987. The estimates are from a linear model fitted to whale-catch records, and are standardized to first 10-day period of January and the longitudinal sector 20°–30° E. The year is defined by the first decade (ten days) in January, and so, for example, 1932 is the mid-point of the 1931/32 season. The predictions are most precise at the centre-of-mass of the data, and so the selected decade and longitude are based on the mean value of each factor weighted by the number of observations at each of its levels. The year effects are corrected for decade and longitude, and so describe a generalized effect for the latitude of catches with time. The actual pattern over time for a given sector and decade would not necessarily correspond exactly to the pattern shown because there are likely to be interactions between the factors. However, these could not be estimated with the data available. The error bars represent ± 1 standard error.

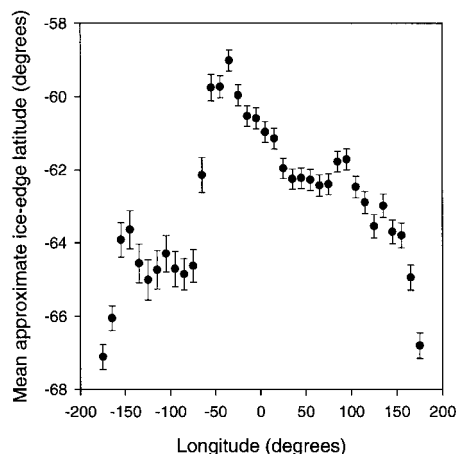


Figure 2 Mean approximate ice-edge latitude in Antarctica by 10° longitudinal sector. The estimates are from a linear model fitted to whale-catch records, and are standardized to the first decade of January and the year 1957. Longitudes to the west are plotted as negative values. The southernmost catches are around 180°W, corresponding to the middle of the Ross Sea. At 70°W the mean catch latitude moves north around the Antarctic Peninsula, and remains at a low latitude across the Scotia Sea. The latitudes move steadily southwards, showing a dip into Prydz Bay at 65°–75° E, and a small bulge at 85° and 95° E corresponding to the West Ice Shelf and Shackleton Ice Shelf, before continuing to trend southwards into the Ross Sea. The error bars represent ± 1 standard error.

shows the longitudinal pattern in the latitudes of the southernmost catches, which reflects the outline of the sea ice around Antarctica. These results show that the analysis captures the major features of the Antarctic sea ice, lending confidence that the pattern in Fig. 1 is a real reflection of trends in Antarctic sea-ice coverage.

Interpretation of Fig. 1 can be improved by analysing the relationship between the noon positions of the factory ships and the ice edge, for which two additional data sets are available: charts of the sea-ice edge⁵ and data compiled³ from Joint Ice Center (JIC) charts, based largely on satellite data. Figure 3a shows the strong correlation between the mean southernmost catch latitudes with the ice-edge data⁵ for the 'years' 1932–39. This ice edge is described as the "close-pack", and is therefore likely to be sea-ice coverage of 80%

Table 1 Analysis of variance for the southernmost catch positions of whales in the Antarctic

Factor	Sum of squares	Degrees of freedom	Mean square	F value	P
Sector	19,688.18	35	562.52	112.97	<0.000001
Decade	22,224.24	18	1,234.68	247.95	<0.000001
Year	4,581.13	37	123.81	24.86	<0.000001
Residual	21,576.43	4,333	4.98		

The southernmost catch position is the dependent variable; $R^2 = 0.683$. The factors are defined in the text.

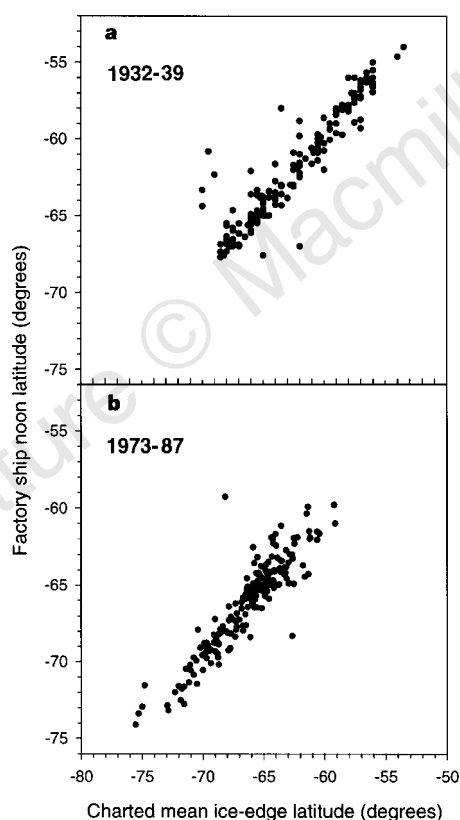


Figure 3 The relationship between the latitudes of the southernmost whale catches, in terms of the factory-ship noon positions, and information on the ice-edge given in charts published in reports⁵ of the Discovery Committee (a) and from data³ derived from charts published by the Joint Ice Center (JIC) (b). The Discovery data cover the 'years' 1932–39, and the JIC data cover 1973–87. There are 178 observations where the Discovery and southernmost-catch data can be compared. A linear regression of the catches on the Discovery data gives $R^2 = 0.88$, with a slope of 0.845 (standard error, 0.024). There are 196 observations where the JIC and southernmost-catch data sets can be compared. The regression of catch positions on the JIC data gives $R^2 = 0.832$, with a slope of 0.875 (standard error, 0.028).

or more. The mean difference between this ice edge and the southernmost catch latitudes is 0.58° (35 nautical miles) with standard error 0.11° (6.5 nautical miles), which is statistically significant ($t = 5.38$, $P < 0.001$). The analysis includes data collected by whaling fleets, which ensures a high degree of correlation, but also constitutes direct evidence of their close proximity to the ice edge. Figure 3b shows the strong correlation between the catch latitudes and the JIC ice-edge data for the period 1973–87. The mean difference between the latitude of the southernmost catches and the JIC ice edge is 0.14° (8.3 nautical miles) to the north (standard error, 0.09°). The whaling latitudes are closer because the JIC ice edge used applies to 15% coverage.

One possible explanation for the change in whaling latitudes is that it is entirely related to the differences in species composition between the blue–humpback–fin era and the later minke era. The use of only the southernmost catches, their high correlation with direct ice-edge observations, the direct descriptions of the relationship between whaling and the ice edge^{7,10,12} and knowledge of the distributions of whales obtained during sightings surveys¹⁴ all show that this explanation can be conclusively rejected. Statistical confounding can also be rejected; there is no systematic shift of any consequence in longitudinal or decadal coverage between the blue–fin–humpback era and the minke era (see Supplementary Information).

The difference between the mean distances from the ice edge to factory-ship positions for the blue–humpback–fin era and the later minke era is almost certainly due largely to the differences in the definitions of the ice edge used in the charts and the compiled³ JIC data. There was no change in whaling technology between the 1950s and 1980s that would allow whaling in heavier ice concentrations in the more recent period. Whale catching requires water that is substantially clear of ice. The positions of factory ships in the minke era are about 5–20 nautical miles north of the 'hard' ice-edge¹². Therefore, the relationship between the southernmost whale catches and the zone where ice becomes too thick for catching is substantially the same in the minke period as it was in the blue–humpback–fin period. If there is a difference, it is certainly less than 0.5° ; too small to account for the changes shown in Fig. 1. Therefore, Fig. 1 indicates real trends in Antarctic sea-ice extent over the period. The mean area of sea ice from 1973 to 1981 was² $17.4 \times 10^6 \text{ km}^2$; 2.8° of latitude at 63°S is an area of $5.65 \times 10^6 \text{ km}^2$, which corresponds to a decline in sea-ice coverage of about 25%.

Figure 1 shows that a substantial decline in sea-ice extent has occurred. Although this has been suggested before^{1,4,6}, the whale-catch records bring much more data to bear, and with circumpolar coverage. They also cover the period 1945–59, during which (apart from ref. 15) few direct observations of the ice edge were reported. The decline occurred relatively quickly, beginning in the mid 1950s, and was largely complete by 1973. Frustratingly, the change pre-dates reliable satellite observations. Based on satellite data, the International Panel on Climate Change concluded that Antarctic sea-ice coverage since 1973 had remained close to average¹⁶. These analyses also show that sea-ice extent has been roughly stable since 1973. However, the abrupt change from the 1950s to the 1970s shows that Antarctic sea-ice extent was not stable before 1973.

A system in which the sea-ice extent seems to be roughly stable and then changes abruptly to again appear roughly stable provides an interesting challenge for coupled atmosphere–ocean general circulation models; analysis of such a system may give insights into fundamental climate processes. The importance of the marginal sea-ice zone in primary production suggests that a decline in Antarctic marine productivity may have already occurred. □

Received 19 November 1996; accepted 9 July 1997.

- Kukla, G. & Gavin, J. Summer ice and carbon dioxide. *Science* **214**, 497–503 (1981).
- Zwally, H. J., Parkinson, C. L. & Comiso, J. C. Variability of Antarctic sea-ice and changes in carbon dioxide. *Science* **220**, 1005–1012 (1983).

3. Jacka, T. H. Antarctic and Southern Ocean sea-ice and climate trends. *Ann. Glaciol.* **14**, 127–130 (1990).
4. Jacka, T. H. & Budd, W. F. in *International Conference on the Role of the Polar Regions in Global Change* (eds Weller, G., Wilson, C. L. & Severin, B. A. B.) 63–70 (Univ. Alaska, Fairbanks, 1991).
5. Mackintosh, N. A. & Herdman, H. F. P. Distribution of the pack-ice in the Southern Ocean. *Discovery Rep.* **19**, 285–296 (1940).
6. Murphy, E. J., Clarke, A., Symon, C. & Priddle, J. Temporal variation in Antarctic Sea-ice: analysis of a long term fast ice record from the South Orkney Islands. *Deep-Sea Res.* **42**, 1045–1062 (1995).
7. Tonneson, J. N. & Johnson, A. O. *History of Modern Whaling* (Hurst, London, 1984).
8. Hart, T. J. On the phytoplankton of the southwest Atlantic and the Bellingshausen sea. *Discovery Rep.* **8**, 1–208 (1934).
9. Smith, W. O. J. & Nelson, D. M. Phytoplankton bloom produced by a receding ice-edge in the Ross Sea: spatial coherence with the density field. *Science* **227**, 163–167 (1985).
10. Hjort, J., Lie, J. & Ruud, J. T. Norwegian pelagic whaling in the Antarctic III. *Hvalradets Skrifter* **8**, 4–36 (1933).
11. Horwood, J. *The Sei Whale: Population Biology, Ecology and Management* (Croom Helm, London, 1987).
12. Shimadzu, Y. & Katabami, Y. A note on the information on the pack ice edge obtained by Japanese catcher boats in the Antarctic. *Rep. Int. Whal. Commis.* **34**, 361–363 (1984).
13. Venables, W. N. & Ripley, B. D. *Modern Applied Statistics with S-Plus* (Springer, New York, 1994).
14. Kasamatsu, F., Joyce, G. G., Ensor, P. & Mermoz, J. Current occurrence of baleen whales in Antarctic waters. *Rep. Int. Whal. Commis.* **46**, 293–304 (1996).
15. Heap, J. *Sea Ice Distribution in the Antarctic between 7° W and 92° W* (Admiralty Hydrographic Off., London, 1963).
16. Nicholls, N. et al. in *Climate Change 1995: The Science of Climate Change* (eds Houghton, J. T. et al.) 137–192 (Cambridge Univ. Press, 1996).

Supplementary Information is available on Nature's World-Wide Web site (<http://www.nature.com>) or as paper copy from Mary Sheehan at the London editorial office of Nature.

Acknowledgements. I thank C. Allison and staff at the International Whaling Commission for compiling these data. I also thank I. Allison, J. Heap, H. Marchant and P. Quilty for comments.

Correspondence and requests for materials should be addressed to the author (e-mail: bill_de@antdiv.gov.au). Southernmost catch records and direct sea-ice data are available on <http://www.antdiv.gov.au/aad/sci/human/aadc/dissemination/dissemination.html>.

Measurements of electric anisotropy due to solidification texturing and the implications for the Earth's inner core

Michael I. Bergman

Physics Department, Simon's Rock College, Great Barrington, Massachusetts, 01230, USA; and Department of Earth and Planetary Sciences, Harvard University, Cambridge, Massachusetts 02138, USA

Seismic body-wave and normal-mode data^{1–4} suggest that the Earth's solid inner core is elastically anisotropic, with the fast direction nearly parallel to the rotation axis. Compressional body-wave data also suggest that the anisotropy increases with turning depth, with a maximum anisotropy of 3–4% (refs 5–7). Here I propose that the inner core's elastic anisotropy and the depth dependence of the anisotropy may be due to solidification texturing that results from the dendritic growth of iron crystals. I demonstrate through laboratory measurements that directionally solidified metallic alloys can indeed exhibit a significant elastic anisotropy due to solidification texturing. The anisotropy is due to the dendrites growing along a particular crystallographic axis^{8,9}, which tends to be aligned along the direction of heat flow. Directional cooling in the Earth's core must therefore be predominantly in the cylindrically radial direction in order for solidification texturing to cause the observed anisotropy; such directional heat flow may be consistent with the pattern of convection in the outer core¹⁰. It is possible that columnar crystals composed of dendrites and elongated in the cylindrically radial direction could also explain observations of inner-core attenuation anisotropy^{11,12}.

The elastic anisotropy of the individual crystals composing the inner core may be responsible for the observed seismic anisotropy if there is a mechanism to align the crystals and cause a preferred orientation, or texturing, of the crystals. Possible mechanisms include deformation texturing due to thermally driven solid-state

convection¹³, and texturing due to solidification in a magnetic field of crystals with an anisotropic paramagnetic susceptibility¹⁴. It has also been suggested that the entire inner core might be a single crystal, obviating the need for an alignment mechanism, and yielding a maximum anisotropy¹⁵. Another possibility is that the pattern of convection in the fluid outer core could lead to latitudinal variations in the inner-core growth rate. Isostatic adjustment via solid-state flow might then relax the inner–outer core boundary towards the equipotential, allowing the development of a deformation or recrystallization texture^{16,17}. Here I discuss another mechanism, directional solidification and the resulting solidification texturing.

When an alloy melt solidifies directionally, a flat interface can become morphologically unstable because of constitutional supercooling⁸. With increasing instability, solvent-rich dendrites form, which make up the mushy zone between liquid and solid. A small temperature gradient and a large solidification front speed favour a thick mushy zone¹⁸. As primary dendrites grow along a particular crystallographic axis^{8,9}, and also tend to grow along the direction of heat flow, a particular crystallographic axis tends to lie in the direction of heat flow, even in a polycrystalline metal^{19,20}. This is solidification texturing. For face-centred cubic (f.c.c.) and body-centred cubic (b.c.c.) metals the axis of primary dendritic growth is $\langle 100 \rangle$, for hexagonal close-packed (h.c.p.) metals the axis is $\langle 210 \rangle$, and for tetragonal metals $\langle 110 \rangle$.

It is thought that the Earth's core is an iron-rich alloy of iron (as well as some nickel) and a lighter constituent, perhaps metallic iron oxide or iron sulphide^{16,21}. Numerical estimates suggest that the inner core may grow dendritically, and that the mushy state may extend deep into the inner core²². There is also meteoritic evidence from presumed planetoid cores that hints at dendritic structures with primary arm spacing of the order of tens of metres (ref. 23), a large length scale that results from the small cooling rate and front speed²⁴. Numerical estimates also suggest that the fluid in the mushy zone beneath the inner–outer core boundary is convecting vigorously²⁵, which is predicted to result in a very high solid fraction except in the very upper reaches of the inner core²⁶. A rapid change in the solid fraction is consistent with seismic reflections off the inner–outer core boundary²⁷, while small fluid inclusions could be responsible for the high overall attenuation of seismic waves in the inner core²⁸.

To examine whether solidification texturing could yield a measurable elastic anisotropy, I studied dendritic growth in a tin-rich alloy. Although tin has a centred tetragonal structure, whereas iron under inner-core pressure and temperature is thought to have either an h.c.p. or an f.c.c. lattice^{15,29}, the solidification-texturing mechanism is essentially the same in all dendritic metallic alloys. I solidified a 97% Sn–3% Pb, 400-g, 35-mm-diameter cylindrical ingot directionally by cooling from beneath (Fig. 1). By alloying the tin with a few per cent lead (f.c.c.) constitutional supercooling and dendritic growth of tin-rich dendrites is promoted¹⁸. Because there is only a low percentage of solute in the original melt, the solidified ingot has only a small percentage of solute-enriched interdendritic material. In the Earth's inner core the percentage of solute-enriched interdendritic material is also small, even though the solute percentage of the core as a whole may be larger, because of fractionation and convection of light solute into the outer core^{22,25}. Although the pressure, temperature, composition, and length and timescales of the experiments differ widely from those in the inner core, I have modelled a high-solid-fraction dendritic zone because such a zone has been predicted to exist even under those very different conditions in the inner core²².

Tin dendrites grow along the $\langle 110 \rangle$ axis, but in the plane perpendicular to dendritic growth a given crystal can be orientated arbitrarily. Thus, even if a polycrystalline tin sample exhibits perfect alignment of the $\langle 110 \rangle$ axes along the direction of heat flow, any orientation in the plane perpendicular to the direction of heat flow